Dalton Transactions

Accepted Manuscript

ROYAL SOCIETY OF CHEMISTRY

www.rsc.org/dalton

Journal Name

ARTICLE

In air a spin crossover active iron(II) complex of amine/$NCBH_3^-$ ligands is converted to a low spin complex of imine/CN^- ligands

Received 00th January 20xx,
Accepted 00th January 20xx

DOI: 10.1039/x0xx00000x

www.rsc.org/

Jian Zhou,[a] Bo-Wen Zhu,[a] Jie Luan,[a] Zhan Liu,[a] Jing-Kun Fang,[a] Xin Bao,[a, b]* Guo Peng,[c] Jiri Tucek,[d] Song-Song Bao[b] and Li-Min Zheng[b]

Two new mononuclear Fe^{II} complexes, $[FeL_1(NCBH_3)_2]$ (**1**) and $[FeL_2(CN)_2]\cdot 3H_2O$ (**2**) (L_1 = N,N'-bis(2-pyridylmethyl)-1,2-ethanediamine, L_2 = N-(2-pyridylmethyl)-N'-(2-pyridylmethylene)-1,2-ethanediamine) were synthesized from the same starting solution under different atmospheric conditions. Complex **1** was isolated in N_2 atmosphere with an expected molecular structure, namely a tetradentate L_1 ligand and two $NCBH_3^-$ co-ligands wrapping an iron(II) ion. It exhibits a gradual spin crossover centered around 355 K, as confirmed by X-ray crystallography, magnetic, DSC and Mössbauer studies. Complex **2** was isolated in the presence of air. One of the secondary amine groups in L_1 undergoes an in-situ oxidative dehydrogenation, forming a new monoimine asymmetric ligand L_2. Besides, CN^- co-ligand is also in-situ generated from $NCBH_3^-$ during the reaction. The strong ligand field strength imposed by CN^- and L_2 stabilizes **2** in LS state. Solvent water molecules in complex **2** are hydrogen bonded into a well-defined 1D water chain. **2** shows a proton conductivity of 8.9×10^{-5} S cm^{-1} at 55 °C and 95 % relative humidity.

Introduction

A fast physical response of materials to external stimuli is highly demanded for the development of switches and sensors. Particularly those accompanied with color change are preferred in real applications. Spin crossover (SCO) complexes represent one of the most attractive molecule based switchable materials. They present different magnetic, optical, electrical and structural properties induced by a variation of temperature, pressure, illumination, magnetic field and gas adsorption.[1,2] The ligand field strength plays a decisive role on the spin state of the metal center, namely, ligands with weak donor character favor the high-spin state (HS) while those with a strong ligand field prefer the low-spin state (LS). In the case of medium donor strength, an entropy-driven SCO from LS to HS is observed. Great efforts have been devoted to obtain SCO complexes through ligand modification.[3] In the meanwhile, a facile regulation on the SCO properties is a goal being pursued. Combining photo-active organic ligand is a promising strategy, taking advantage of a facile change of the ligand field strength induced by photoisomerization.[4,5] In addition, the extreme sensitivity of SCO behavior to very subtle effects offers an opportunity to perturb the spin state through guest and solvent inclusion.[6]

Solid-state proton (H^+) conductors have attracted considerable interest due to their potential applications in fuel cells, hydrogen sensing and electrochemical production of hydrogen.[7] Compared with typical amorphous organic polymers, well-defined crystalline complexes allow for direct visualization of the proton conduction pathways and mechanism. Metal–organic frameworks (MOFs) have recently been extensively investigated as promising candidates for proton-conductors, as their crystallinity, tailorable porosity and dynamic behavior provide various methods to optimize the performance.[8] Different types of organic linkers, such as oxalic,[9] carboxylic[10] and phosphonic acid[11] have been exploited to construct MOFs with high proton conductivity. In addition, loading of proton carriers, such as water, NH_4^+,[12, 9b] $[(CH_3)_2NH_2]^+$,[13] imidazole[14] and 1,2,4-triazole[15] has proved to be an effective strategy to improve the proton conductivity. On the other hand, discrete metallosupramolecular complexes may serve as an alternative choice to promote the discovery of new solid proton conducting materials, which have complementary properties to MOFs such as better solubility in common solvents and easy processing. However, to the best of our knowledge, only two discrete metallosupramolecular architectures have been reported to show proton conductivity.[16]

We have recently reported a mononuclear iron(II) complex $[Fe(^{Me}L_1)(NCSe)_2]$ ($^{Me}L_1$ = N,N'-dimethyl-N,N'-bis(2-

[a] School of Chemical Engineering, Nanjing University of Science and Technology, 210094 Nanjing, P. R. China.
[b] State Key Laboratory of Coordination Chemistry, Coordination Chemistry Institute, School of Chemistry and Chemical Engineering, Nanjing University, Nanjing 210093, P. R. China.
[c] Herbert Gleiter Institute of Nanoscience, Nanjing University of Science and Technology, 210094 Nanjing, P. R. China.
[d] Regional Centre of Advanced Technologies and Materials, Department of Experimental Physics, Faculty of Science, Palacky University, Slechtitelu 11, 783 71 Olomouc, Czech Republic.

† Footnotes relating to the title and/or authors should appear here.
Electronic Supplementary Information (ESI) available: [ESI-MS spectrum for complex **2**, experimental procedures, crystallographic data and molecular structures of $[NiL_1(NCBH_3)_2]$]. See DOI: 10.1039/x0xx00000x

pyridylmethyl)-1,2-ethanediamine) showing polymorphism dependent magnetic properties.[17] One of the polymorphs exhibits intriguing hysteretic two-step spin transition with an ordered [HS–HS–LS] intermediate phase. However, the transition takes place in quite low temperature range (90–110 K), which hampers its application at ambient conditions. A related tetradentate ligand N,N'-bis(2-pyridylmethyl)-1,2-ethanediamine (L_1) has also been exploited to construct SCO complexes together with NCS^{-}[18] and $NCSe^{-}$[19] co-ligands, showing SCO equilibrium centered around 70 and 180 K, respectively. The occurrence of SCO in those complexes indicates the appropriate ligand field strength imposed by such type of ligand. We herein are motivated to further improve the transition temperature toward room temperature by using an even stronger donor $NCBH_3^-$. To our surprise, the final product is dependent on the reaction conditions (Scheme 1): the expected SCO complex $[FeL_1(NCBH_3)_2]$ (**1**) can only be isolated in N_2 atmosphere; exposure of the solution to air leads to a rapid color change from yellow to violet, which gives a LS complex $[FeL_2(CN)_2]\cdot 3H_2O$ (**2**). Single crystal diffraction analysis, MS and IR spectra confirm an in-situ oxidative dehydrogenation of L_1 as well as a generation of CN^- from $NCBH_3^-$ during the conversion from **1** to **2**.

Scheme 1. Synthetic routes of **1** and **2**.

Results and Discussion

Syntheses and ESI-MS Studies

Evaporation of the MeOH/MeCN solution of L_1, $Fe(ClO_4)_2\cdot 6H_2O$, and $NaNCBH_3$ in N_2 atmosphere gave orange flaky crystals of **1**. Once the reaction mixture was exposed in air, the yellow solution turned dark immediately and finally became violet (Figure 1). Rectangular prism violet crystals of **2** were obtained by evaporation of the violet solution. It should be mentioned that the conversion from **1** to **2** was only observed in solution; complex **1** is quite stable in the solid state.

The dehydrogenation of L_1 ligand and the decomposition of the $NCBH_3^-$ co-ligand in complex **2** were confirmed by electrospray ionization mass spectrometry (ESI-MS) (Figure S1). The only intense peak at *m/z* 321.98 with isotopic distributions corresponds to $[FeL_2(CN)]^+$ (calc.: 322.08).

IR spectra

Solid-state infrared (IR) spectra were recorded for **1** and **2** at room temperature (Figure 2). The characteristic bands of N–H, B–H and C≡N stretches in complex **1** were observed around 3232, 2330 and 2203 cm^{-1}. By contrast complex **2** shows a distinct spectrum, in accordance with the occurrence of the changes in the ligands. The band around 1638 cm^{-1} unambiguously confirms the formation of C=N bond. The remaining N–H stretch is covered by the strong H_2O absorption centered around 3252 cm^{-1}. The band at 2070 cm^{-1} was assigned to terminal cyanide ion coordinating to LS Fe^{II}.[20]

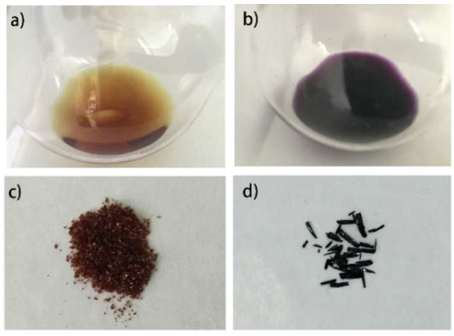

Figure 1. Photo images showing the color change of the solution before (a) and after (b) exposed in air; photo images of crystals of **1** (c) and **2** (d).

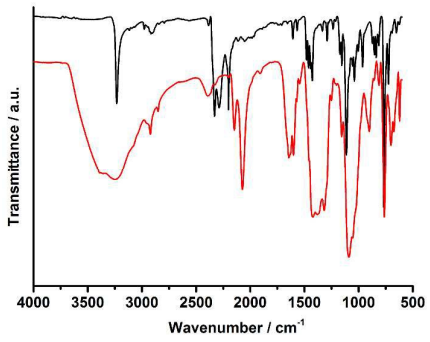

Figure 2. Room temperature IR spectra for **1** (black) and **2** (red) in the region of 4000–600 cm^{-1}.

Journal Name

ARTICLE

Table 1. Unit cell and selected refinement parameters for **1** and **2**.

	1		**2**
Temperature / K	150	373	298
Empirical formula	$C_{16}H_{24}B_2FeN_6$	$C_{16}H_{24}B_2FeN_6$	$C_{16}H_{20}FeN_6O_3$
Formula weight / g mol^{-1}	377.88	377.88	400.22
Crystal system	Orthorhombic	Orthorhombic	Triclinic
Space group	*Aba*2	*Aba*2	*P*-1
***a* / Å**	14.3553(8)	14.3196(18)	7.3852(12)
***b* / Å**	15.2389(11)	15.4416(14)	11.0858(18)
***c* / Å**	8.8543(7)	9.4510(10)	11.913(2)
α / °	90	90	105.378(2)
β / °	90	90	91.266(3)
γ / °	90	90	101.044(3)
Volume / Å^3	1937.0(2)	2089.8(4)	920.2(3)
Z	4	4	1
ρ_{calc} / mg mm^{-3}	1.296	1.201	1.4443
μ / mm^{-1}	0.789	0.731	0.848
***F*(000)**	792	792	416.9
Reflections collected	6315	6699	6665
Independent reflections	1510	2319	4556
	R_{int} = 0.0436	R_{int} = 0.0395	R_{int} = 0.0242
Goodness-of-fit on F^2	1.044	1.06	1.057
Final *R* indexes	R_1 = 0.0294	R_1 = 0.0403	R_1 = 0.0349
[$I \geq 2\sigma(I)$]	wR_2 = 0.0591	wR_2 = 0.0728	wR_2 = 0.0906
Final *R* indexes	R_1 = 0.0420	R_1 = 0.1010	R_1 = 0.0408
[all data]	wR_2 = 0.0630	wR_2 = 0.1001	wR_2 = 0.0954
Largest diff. peak/hole / e Å^{-3}	0.18/-0.18	0.23/-0.23	0.48/-0.53
Flack parameter	0.04(4)	0.00(3)	

Table 2. Selected bond lengths and angles for **1** and **2**.

	1		**2**
Temperature / K	150	373	298
Fe–N_{NCBH3} / Å	1.938(4)	2.043(6)	
Fe–N_{py} / Å	1.977(2)	2.14	1.9519(15), 2.0028(14)
Fe–N_{amine} / Å	2.009(4)	2.14	2.0099(16)
Fe–N_{imine} / Å			1.8918(16)
Fe–C_{CN} / Å			1.9197(19), 1.9357(17)
Fe–$N_{average}$ / Å	1.97	2.11	1.96
C=N / Å			1.286(3)
C–N / Å	1.484(6)	1.49	1.478(3)
***cis* N–Fe–N / °**	83.38(16)–94.36(15)	76.4(8)–96.6(12)	80.87(6)–94.18(6)
***cis* N–Fe–C / °**			89.67(6)–98.16(6)
***cis* C–Fe–C / °**			88.54(7)
***trans* N–Fe–N / °**	170.9(2)–178.2(4)	170.5(15)–178.7(7)	165.35(6)
***trans* N–Fe–C / °**			174.59(7)–178.81(7)
Σ_{Fe} / °	34.4	61.4	51.1
N–C–B / °	179.4(4)	179.3(8)	
Fe–N≡C / °	178.2(4)	178.7(7)	177.9(2), 178.57(15)

Crystal Structure Analysis

The single crystal structures were determined at 150 K (LS phase) and 373 K (close to HS phase) for **1** and at 298 K for **2**. The crystallographic data and refinement parameters are listed in Tables 1 and 2. Complex **1** crystallizes in the orthorhombic space group *Aba*2 while **2** crystallizes in the triclinic space group *P*-1. The asymmetric unit of **1** contains half of the molecule with a 2-fold axis passing through the Fe^{II} atom. As shown in Figure 3, the ligand adopts a *cis*-α conformation with the pyridine groups in the axial positions, leaving two *cis* positions for $NCBH_3^-$ co-ligands. The Fe–N≡C angle is almost linear (178.2(4)^o at 150 K), implying a strong ligand field strength imposed by $NCBH_3^-$. The Fe–N_{NCB} bonds are the shortest while the Fe–$N_{aliphatic}$ bonds are the longest, consistent with literature reports of related complexes.[17,18,21] Aliphatic N atom is incapable of forming π-backbonding, resulting in a weakening of coordination bond when compared with other N atoms located in a conjugated environment. At 150 K, the average Fe–N bond length 1.97 Å is typical for Fe^{II} ion in the LS state. Upon warming to 373 K, the average Fe–N bond length increases dramatically to 2.11 Å, indicating the predominance of Fe^{II} ion in the HS state. The variation of the octahedral distortion parameter Σ is also an effective indicator for the occurrence of SCO.[22] The value increases from 34.4^o at 150 K to 61.4^o at 373 K, in accordance with smaller Σ in the LS state and bigger Σ in the HS state. As shown in Figure 4, homochiral molecules (Δ-*cis*-α) pack in the *bc* plane via B···C (3.406(6) Å at 150 K) and B···H (2.66(3) Å at 150 K) Van der Waals interactions, forming a 2D chiral layer. In the *ac* plane, molecules with opposite chirality stack alternatively through C···H short contacts (2.63–2.80 Å at 150 K), resulting in the overall racemic complex.

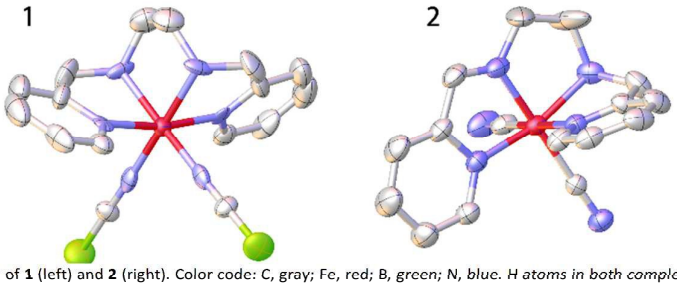

Figure 3. View of the molecular structures of **1** (left) and **2** (right). Color code: C, gray; Fe, red; B, green; N, blue. H atoms in both complexes and water molecules in **2** are omitted for clarity.

In complex **2**, L_1 ligand undergoes an in-situ oxidative dehydrogenation. One of the two C–N bonds is dehydrogenated to form a C=N bond, which is undoubtedly corroborated by the short C–N distance (1.286(3) Å). In contrast, the remaining C–N_{amine} bond has an obviously longer bond length of 1.478(3) Å. Fe ion locates in a distorted [N_4C_2] octahedral environment provided by a L_2 ligand and two CN^-. The tetradentate L_2 ligand adopts a *cis*-β conformation due to the presence of both sp^2 and sp^3 hybridization. The remaining two coordination sites are occupied by C atoms from two CN^- ligands, which are in-situ generated from $NCBH_3^-$. The Fe–N bond lengths cover the range 1.89–2.01 Å, among which Fe–N_{imine} is the shortest and Fe–N_{amine} the longest. The average Fe–C bond length is 1.92 Å. The metal ion can be assigned to LS Fe^{II} based on charge balance and bond length.

The metal center is chiral due to the *cis*–β arrangement of the tetradentate L_2 ligand. As shown in Figure 5, molecules with opposite chirality stack alternatively in the *bc* plane through N···H (2.22–2.64 Å), C···H (2.749(2) Å) and π···π interactions (distance between plane centroids: 3.6167(16) Å), forming a 2D flat layer with pockets. The cyanide groups point to the pocket and anchor solvent water molecules through N···H (1.98–2.11 Å) hydrogen bonds. Such hydrogen bonds may allow the water protons to become more acidic. The water molecule positions are fully occupied and well-resolved in the X-ray structure. Each water molecule is hydrogen bonded to the adjacent ones, forming a tape of alternate 4- and 6-membered rings sharing one edge and running along the *a* axis (Figure 5c). The topology of the water network can be classified as T4(2)6(2) according to ref 23. The oxygen atoms in the 4-membered rings are in a plane while those in the 6-membered rings display a chair conformation. O···O distances are in the range of 2.88–2.90 Å and the O–H···O angles (169.35–173.36^o) are quite close to 180^o. The 2D layers are further linked together by inter-layer N···H (2.7201(36) Å) hydrogen bonds, forming a 3D close packed supramolecular network (Figure 5d).

Journal Name

ARTICLE

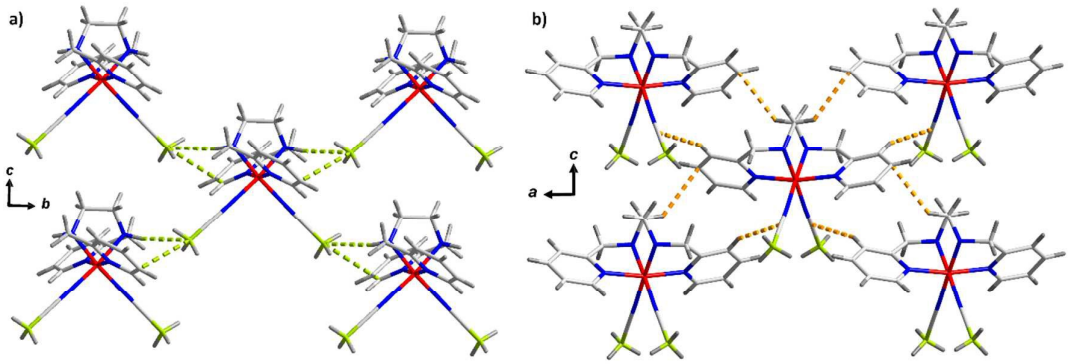

Figure 4. Packing diagrams of **1** showing the homochiral layer packed in the *bc* plane (a) and the heterochiral layer packed in the *ac* plane (b). Color code: C, light gray; H, gray; Fe, red; N, blue; B, green. Short interactions are indicated in dotted lines.

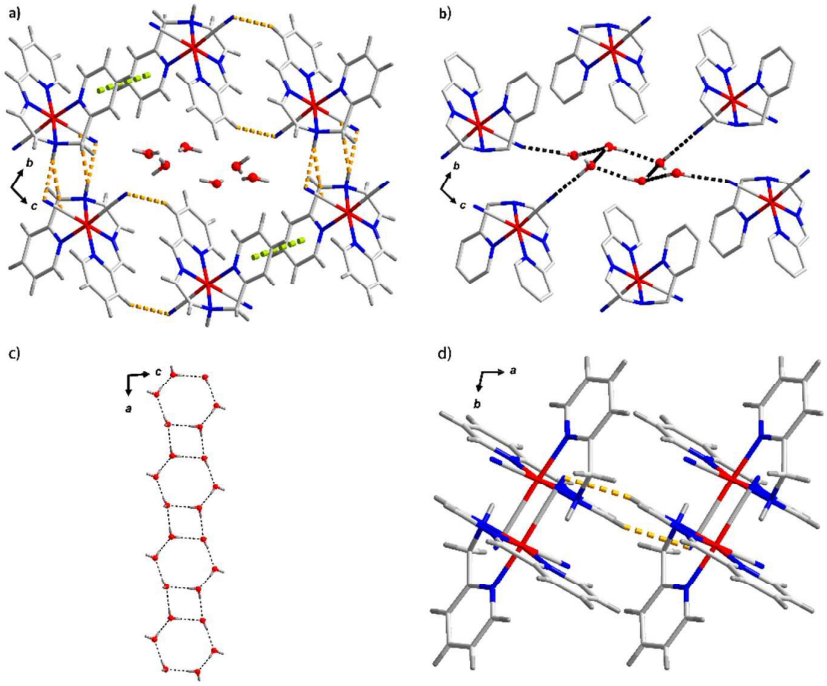

Figure 5. Packing diagrams of **2**: (a) 2D supramolecular layer in the *bc* plane linked through abundant supramolecular interactions. (b) View of hydrogen bonds between cyanide groups and solvent water molecules resided in the pocket. H atoms in the L_2 ligand are omitted for clarity. (c) View of the hydrogen-bonded water column running along the *a* axis. (d) Hydrogen bonds formed between *bc* layers. Color code: C, light gray; H, gray; Fe and O, red; N, blue. Short interactions are indicated in dotted lines.

Magnetism

Magnetic susceptibility measurements were carried out on polycrystalline samples of **1** and **2** with an applied magnetic field of 3000 Oe in the temperature range of 10–400 K and 10–300 K, respectively. The results are shown in Figure 6a in the form of $\chi_M T$ versus T plots, where T is the absolute temperature and χ_M is the molar magnetic susceptibility. For complex **1**, the $\chi_M T$ value is 0.08 cm^3 K mol^{-1} at 10 K and then

slowly increases to 0.26 cm^3 K mol^{-1} at 275 K, lying in the range typically observed for Fe^{II} in the LS state. Upon warming, the $\chi_M T$ value continuously increases to 3.00 cm^3 K mol^{-1} at 400 K, implying that most of Fe^{II} ions are in the HS state. A 3 K hysteresis was detected in the subsequent cooling mode but this may not be real.[6k, 24] The $T_{1/2}$ value at which temperature that 50% Fe^{II} ions undergo SCO is c.a. 356 K in the warming mode and 353 K in the cooling mode. The $\chi_M T$ vs T curve for **2** confirms the diamagnetic nature of Fe^{II}, in good agreement with the single crystal analysis. Removal of solvent water molecules doesn't change its diamagnetic nature (Figure S6). The strong ligand field strength imposed by CN^- and L_2 ligands stabilizes the metal center in the LS state.

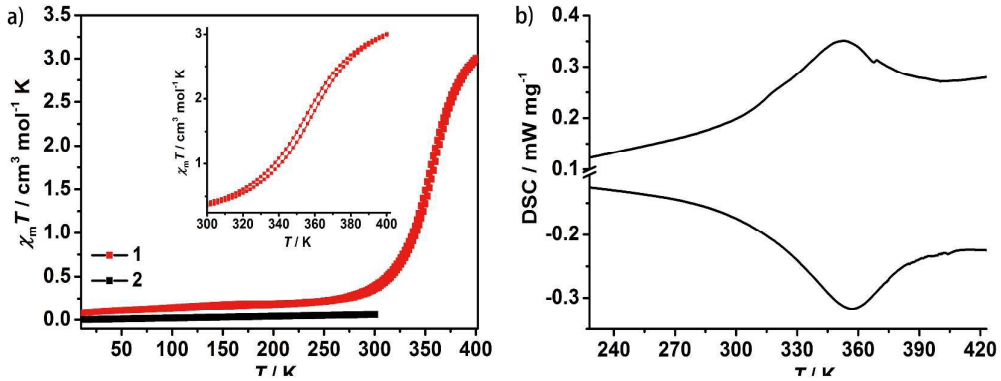

Figure 6. (a) Variable-temperature magnetic susceptibility studies of **1** and **2**. Data recorded in both cooling and heating modes at a scan rate of 2 K min^{-1}. The inset shows the enlarged plot over the temperature range 300–400 K for complex **1**. (b) DSC curve of **1** recorded in both cooling and heating modes over the temperature range 223–433 K.

DSC

DSC measurement for complex **1** was carried out over the temperature range 223–433 K. As shown in Figure 6b, upon heating/cooling at 10 K min^{-1}, heat anomalies of endothermic/exothermic peaks were observed at 356/353 K. These peak temperatures agree well with the transition temperatures observed in the magnetic measurement. The corresponding ΔH values were estimated to be 14.96/-15.04 kJ mol^{-1}. The corresponding ΔS values were estimated to be 42.02/-42.60 J K^{-1} mol^{-1}. These values are within the experimental range generally observed for Fe^{II} SCO complexes.[25]

^{57}Fe Mössbauer Spectra

^{57}Fe Mössbauer spectra of **1** were recorded at 80 and 500 K in the warming mode (Figure 7 and Table S1). At 80 K, only a singlet component was observed with the value of the isomer shift δ = 0.46 mm s^{-1} falling within the range expected for Fe^{II} in a LS state. At 500 K, a doublet corresponding to HS Fe^{II} dominates the spectrum. The isomer shift and quadrupole splitting are δ = 1.35 and ΔE_Q = 1.92 mm s^{-1}, respectively. The spectral fraction of the singlet is at the detection limit of the Mössbauer technique. Thus, the spin transition is almost completed at this temperature.

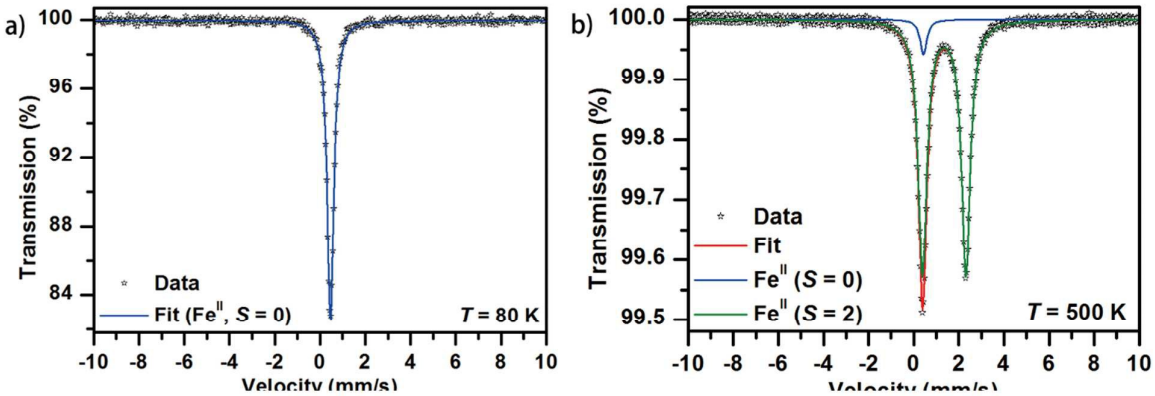

Figure 7. ^{57}Fe Mössbauer spectra of **1** recorded at 80 K (a) and 500 K (b) in the warming mode. The spectra are deconvoluted into HS (green line) and LS (blue line) sites.

Thermogravimetric Analysis

The thermal stabilities of the two complexes were examined by thermogravimetric analysis (TGA) (Figure 8). The TG curve of complex **1** shows that it is stable up to 250 °C. No weight loss was observed before decomposition, confirming the absence of solvent molecule. The initial mass loss of c. a. 7%

between 250-280 °C is probably related to the elimination of two BH_3 units. Time dependent TG curve of **2** (Figure S7) shows the solvent molecules are quite stable at 30 °C. The mass loss starts above 30 °C and then reaches a plateau around 100 °C. Weight loss (13.8%) during this temperature range corresponds to the elimination of three water molecules per Fe^{II} ion (theoretical value: 13.5%). The desolvated sample is stable up to 270 °C, followed by decomposition upon further heating.

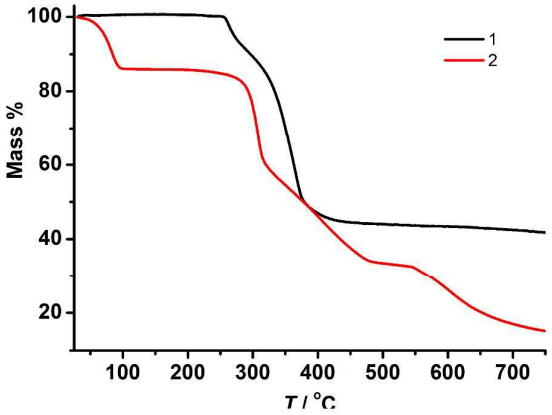

Figure 8. TG curves for **1** and **2**.

PXRD

The crystalline phase purity of the as-synthesized samples **1** and **2** was confirmed by PXRD experiments, which are in good agreement with the simulated patterns (Figure 9). The pattern of **2** remained intact after kept in a humidity oven at 95 % relative humidity (RH) for 24 hours. Moreover, **2** keeps its structure and crystallinity after losing solvent water molecules.

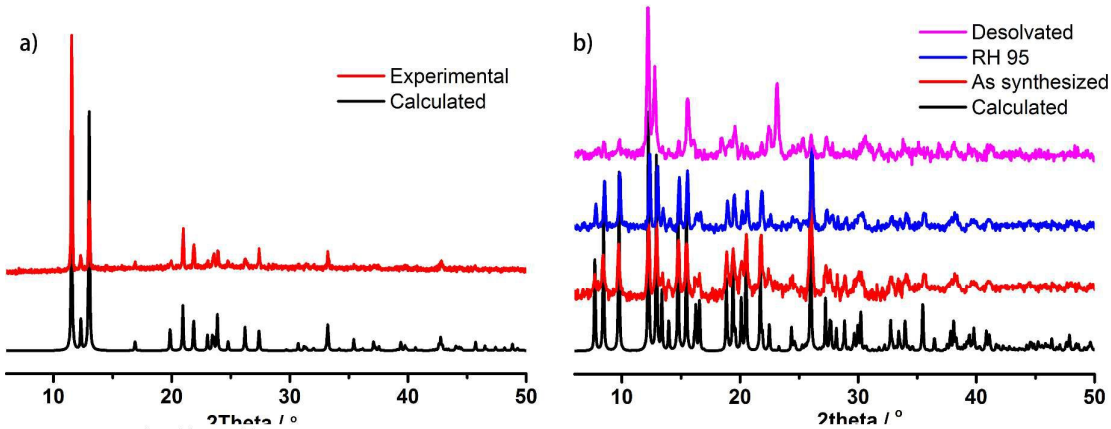

Figure 9. Powder-XRD patterns for **1**(a) and **2**(b).

Proton Conductivity

Inspired by the structural feature of complex **2**, its proton conductivity was measured by AC impedance spectroscopy using a compacted pellet of the powder sample with two gold electrodes attached to the surface. The humidity-dependent proton conductivity was determined at 25 °C in the RH range of 40% to 95%. The conductivities were determined from the semicircle in the Nyquist plots, which are shown in Figure 10a. The log(σ/S cm^{-1}) versus RH profile is given in Figure 10b. These values are highly humidity dependent and dropped from 8.3×10^{-6} at 95% RH to 1.2×10^{-11} at 40% RH, suggesting that water molecules play an important role in creating the proton-conducting pathways.

Journal Name

ARTICLE

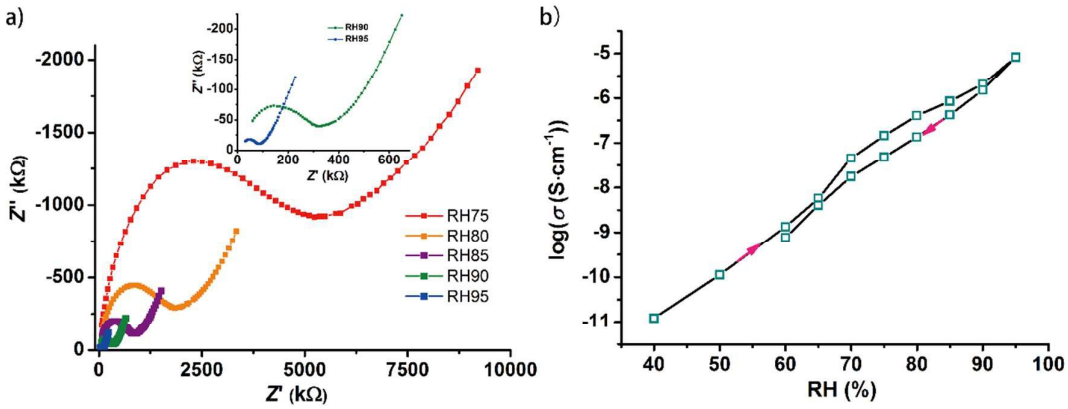

Figure 10. (a) Nyquist plots for **2** at 25 °C and various RH conditions. In the inset the spectra acquired at 95% and 90% RH are shown enlarged. (b) Plot of log(σ) vs RH at 25 °C for **2**.

Temperature dependence of the conductivity was measured from 15 to 55 °C at 95% RH for **2**. The Nyquist plots are shown in Figure 11a. The proton conductivity increases with temperature, from 2.0×10^{-6} at 15 °C to 8.9×10^{-5} at 55 °C. The activation energy (Ea) for the proton migration was calculated according to the Arrhenius equation,

$$\sigma T = \sigma_0 \exp(-Ea/k_B T)$$

where σ is the ionic conductivity, σ_0 is the preexponential factor, k_B is the Boltzmann constant, and T is the temperature. The value of Ea was found to be 0.79 eV. The Grotthuss mechanism is likely to occur in this well-defined 1D water chain pathway. However, the high activation energy suggests the involvement of some other processes such as direct diffusion of additional protons with water molecules (vehicle mechanism).[9d, 26]

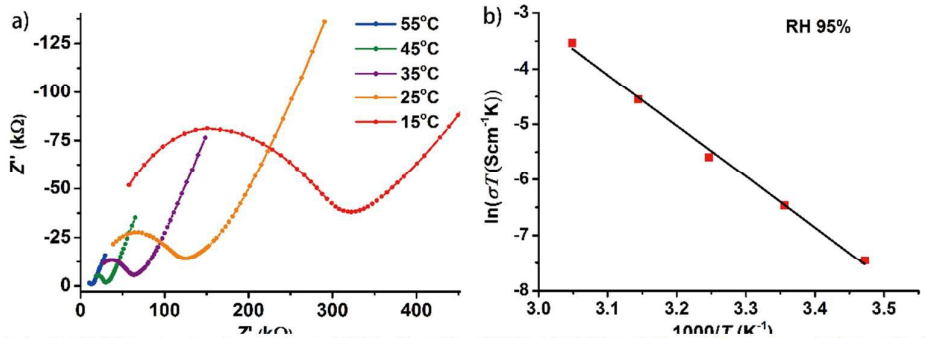

Figure 11. (a) Nyquist plots for **2** at 95% RH and various temperatures. (b) Plot of log(σT) vs $1000/T$ at 95% RH for **2**. *The solid line represents the best fit of* the data.

Discussion

Dehydrogenation of secondary amines to imines, along with the reverse process, is a subject of current interest. It has been found that the presence of transition metal ions can activate amine oxidation.[27] The reactivity of the complex is sensitive to the nature of the ligand and to the identity of the metal. In some literatures the central metal ion acts as oxidant and is reduced via oxidation of the ligand.[27d–f] It is obvious in our case that O_2 is the oxidant and the valence of the metal center remains unchanged. However, Fe^{II} still plays an important role in the occurrence of the reaction. Replacement of Fe^{II} by Ni^{II} results in the isolation of an unoxidized complex that is isostructural to **1** (see the molecular structure and crystallographic data in the supporting information), no matter the presence of O_2 or not. Besides, probably the in-situ decomposition of $NCBH_3^-$ to CN^- is necessary for the oxidation process, since dehydrogenation of the same tetradentate ligand has not been reported when using similar co-ligands such as NCS^- [18b]. To the best of our knowledge, no in-situ reaction involving decomposition of $NCBH_3^-$ to CN^- has been reported before. In order to reveal the role of $NCBH_3^-$ co-

ligand during the formation of **2** we have carried out additional ESI-MS measurement (Figure S2 and S3) for the reaction mixture. The strongest peak detected immediately after mixing the reactants corresponds to $[FeL_1(NCBH_3)]^+$, indicating complex **1** is the major product. A very weak peak corresponding to $[FeL_1(CN)]^+$ was also observed. 5 minutes later the peak of $[FeL_1(NCBH_3)]^+$ became weaker while $[FeL_1(CN)]^+$ became the strongest one. In addition, a very weak peak of $[FeL_2(CN)]^+$ was detected. The results indicate that the in-situ decomposition of $NCBH_3^-$ to CN^- occurs in prior to the dehydrogenation of L_1. Similar to other reports for ligand having more than two amine donors,[27a, d-g] only one of the C–N bonds is dehydrogenated to form a C=N imine bond. Further dehydrogenation of the second C–N bond was not observed under the given experimental condition.

A systematically substitution of the NCE^- (E = S, Se, BH_3) co-ligands usually allows tuning SCO properties in a predictable way. A shift of $T_{1/2}$ toward higher temperature is expected on going from NCS^-, $NCSe^-$ and $NCBH_3^-$. $[FeL_1(NCS)_2]$ was reported to show a SCO equilibrium around 70 K and the residual HS fraction is highly dependent on cooling speed.[18] $[FeL_1(NCSe)_2]$ exhibits a gradual and complete spin transition between 140 and 250 K.[19] However its structure has not been confirmed by crystallographic analysis. Recently we have obtained two polymorphs of $[Fe^{Me}L_1(NCSe)_2]$, where $^{Me}L_1$ is a methyl substituted analogue of L_1.[17] One of the two polymorphs remains HS over all temperatures whereas the other one undergoes a cooperative two-step SCO between 90 and 110 K, accompanied by a cell tripling in the intermediate phase. As expected complex **1** shows an increased transition temperature above room temperature, consistent with the stronger ligand field strength provided by $NCBH_3^-$. It should be noted that although **1** and the SCO polymorph of $[Fe^{Me}L_1(NCSe)_2]$ crystallize in the same space group and have comparable crystal packings, their SCO properties are different in both transition steps and cooperativities. Such phenomenon has also been observed in $[Fe(Rbabpy)(NCS)_2]$ (babpbpy = N_6,N_6′-di(pyridin-2-yl)-2,2′-bipyridine-6,6′-diamine) series.[28] It has been well acknowledged that SCO behavior is quite sensitive to subtle changes in supramolecular interactions. Due to the substitution of $NCSe^-$ by $NCBH_3^-$and CH_3 group by H, some differences come up in the coordination geometries and supramolecular packings. Comparing their structures in HS phase, the Fe–N≡C angle in **1** is much closer to linear (178.5(7)°) than $[Fe^{Me}L_1(NCSe)_2]$ (168.8(5)°). The nearest neighboring Fe···Fe distances are longer in **1** (8.4332(9) vs 8.01111(9) Å), which may explain its weaker cooperativity. In complex **1** interaction between B and H on the secondary amine was found. While in $[Fe^{Me}L_1(NCSe)_2]$ no such hydrogen bond was observed due to the substitution of H by methyl group. Those subtle differences may contribute to their different SCO behaviors.

Conclusions

An in-situ conversion from **1** to **2** was observed in solution in the presence of O_2. The oxidative dehydrogenation of the tetradentate ligand as well as a generation of CN^- from $NCBH_3^-$ were unambiguously confirmed by single crystal diffraction analysis, MS and IR spectra. Consequently the ligand field strength is significantly altered, resulting in different magnetic properties for **1** and **2**: **1** shows gradual SCO above room temperature while **2** stays in the LS state. Moreover, complex **2** provides a rare example of discrete architectures exhibiting proton conductivity. The well-organized 1D water chain running in the intermolecular channel/pocket offers an efficient proton conducting pathways.

Experimental Section

Materials and General Procedures

All reagents obtained from commercial sources were used without further purification. The tetradentate ligand N,N′-bis(2-pyridylmethyl)-1,2-ethanediamine (L_1) was prepared according to the literature.[29]

Variable-temperature magnetic susceptibility measurements were recorded at a rate of 2 K min-1 with a Quantum Design PPMS-9, operating with an applied field of 3000 Oe at temperatures between 10–400 K. Experimental susceptibilities were corrected for diamagnetism of the constituent atoms by the use of Pascal's constants. PXRD patterns were recorded on a D8 ADVANCE X-Ray Diffractometer (Kα radiation, λ = 0.154056 nm). The ^{57}Fe Mössbauer spectra were measured in a transmission geometry employing a Mössbauer spectrometer operating in a constant acceleration mode and equipped with 50 mCi ^{57}Co(Rh) source. For low-temperature measurements, the sample was placed inside a chamber of the closed-helium cycle system and kept under N_2 atmosphere. For high temperature measurements, the sample was placed inside the oven with N_2 atmosphere. The recorded Mössbauer spectra were analyzed using the MossWinn software package. The isomer shift values are referred to metallic α-Fe at room temperature. Elemental analyses were performed using a Elementar Vario EL Elemental Analyser. The IR spectra were recorded from KBr disc in the range 4000-600 cm^{-1} with a Perkin-Elmer Spectrum. DSC measurement was performed on a METTLER TOLEDO DSC1 instrument under nitrogen atmosphere at a scan rate of 10 K min^{-1} in both heating and cooling modes. The carbon, hydrogen, and nitrogen microanalyses were carried out with an Elementar Vario-ELCHNS elemental analyzer. TG analyses were recorded on a Mettler-Toledo TGA/SDTA851^e thermoanalyzer by being filled into alumina crucibles under N_2 atmosphere within the temperature range of 300−1050 K at a heating rate of 10 K min^{-1}.

Proton Conductivity Measurements

AC conductivities were measured using sample pellet (3 mmϕ). The thickness of the pellet was determined as 0.43 mm. Both round faces of sample pellet were treated with gold paste. The impedance measurements were carried out under multiple different environmental conditions by the conventional quasi-four-probe method, using gold paste and gold wires (50 μmϕ) with a Solartron SI 1260 Impedance/Gain-Phase Analyzer and

1296 Dielectric Interface in the frequency range 1 MHz–1 Hz. Humid environments at different temperatures were controlled by using an GDW-100 (Su-Ying Corp.) humidity oven. Data points were taken after the samples appearing to be equilibrated, with no deviation within one hour; this took on the order of 1 day per point.

Single crystal X-ray diffraction

Single-crystal X-ray data were collected on a Bruker D8 Quest diffractometer or a Rigaku R-AXIS SPIDER IP diffractometer using graphite mono-chromated Mo Kα radiation (λ = 0.71073 Å). A multi-scan absorption correction was performed. The data of **1** at two temperatures were collected using different crystals. The reproducibility of the results was confirmed by cell measurements at both temperatures with several crystals. The structures were solved using direct methods and refined by full-matrix least-squares on F2 using SHELXS and SHELXL 2 and the graphical user interface Olex2.3 Non-hydrogen atoms were refined anisotropically and hydrogen atoms were placed in calculated positions refined using idealized geometries (riding model) and assigned fixed isotropic displacement parameters. CCDC-1414293-1414296 contain the supplementary crystallographic data for this paper. These data can be obtained free of charge from The Cambridge Crystallographic Data Centre via www.ccdc.cam.ac.uk/data_request/cif.

Caution! The perchlorate salt used in this study is potentially explosive and should be handled with care. The conversion of $NCBH_3^-$ to CN^- may have significant hazards during the sythesis of **2**.

Synthesis

$[FeL_1(NCBH_3)_2]$ (**1**). To a solution (3 mL MeOH and 2 mL MeCN) of L_1 (L_1 = N,N'-bis(2-pyridylmethyl)-1,2-ethanediamine, 0.024g, 0.1mmol) was added $Fe(ClO_4)_2 \cdot 6H_2O$ (0.036g, 0.1 mmol) and $NaNCBH_3$ (0.013g, 0.2mmol) in a nitrogen atmosphere. The resulting reation mixture was stirred for 10 min and the yellow solution was evaporated in a nitrogen gas stream for 12 h. Orange flaky crystals were obtained in 50% yield (0.019 g). IR (KBr, cm^{-1}): 3232 (N-H), 2330 (B-H), 2203 (C≡N), 1605, 1423, 1109, 751, 721. Elemental analysis, Calcd: C, 50.42; H, 6.41; N, 22.22. Found: C, 50.07; H, 6.37; N, 21.92.

$[FeL_2(CN)_2]\cdot 3H_2O$ (**2**). To a solution (3 mL MeOH and 2 mL MeCN) of L_1 (0.024g, 0.1mmol) was added $Fe(ClO_4)_2 \cdot 6H_2O$ (0.036g, 0.1 mmol) and $NaNCBH_3$ (0.013g, 0.2mmol) without N_2 protection. The resulting reaction mixture was stirred for 1 h in air. The deep violet solution was evaporated in 1 month. Rectangular prism violet crystals of **2** were obtained in 60% yield (0.024g). Dissolving crystals of **1** in MeOH/MeCN and then evaporating it

in air also result in the formation of **2** in 45% yield. IR (KBr, cm^{-1}): 3252 (H_2O), 2928, 2845, 2394, 2148, 2070 (C≡N), 1638 (C=N), 1400, 1317, 1086, 907, 705, 698. Elemental analysis, Calcd: C, 47.78; H, 5.51; N, 20.89. Found: C, 47.43; H, 5.54; N, 20.82.

Acknowledgements

This work was supported by the National Natural Science Foundation of China (21401104), the Natural Science Foundation of Jiangsu Province (BK20140774), the Fundamental Research Funds for the Central Universities (30920140111002), financial support from State Key Laboratory of Coordination Chemistry of Nanjing University and the Zijin Intelligent Program of NJUST.

References

1 (a) O. Kahn and C. J. Martinez, *Science*, 1998, **279**, 44-48. (b) P. Gütlich, Y. Garcia and T. Woike, *Coord. Chem. Rev.*, 2001, **219**, 839-879. (c) P. Gütlich, V. Ksenofontov and A. B. Gaspar, *Coord. Chem. Rev.*, 2005, **249**, 1811-1829. (d) J. A. Real, A. B. Gaspar and M. C.Muñoz, *Dalton Trans.*, 2005, 2062-2079. (e) O. Sato, J. Tao and Y.-Z. Zhang, *Angew. Chem. Int. Ed.*, 2007, **46**, 2152-2187.

2 (a) P. Gütlich and H. A. Goodwin, Spin Crossover in Transition Metal Compounds I–III; Topics in Current Chemistry, Vols. 233–235; Springer: Berlin, Heidelberg, Germany, 2004. (b) A. Bousseksou, G. Molnár and G. Matouzenko, *Eur. J. Inorg. Chem.*, 2004, 4353-4369. (c) A. Bousseksou, G. Molnár, L. Salmon and W. Nicolazzi, *Chem. Soc. Rev.*, 2011, **40**, 3313-3335. (d) M. A. Halcrow, Spin-crossover Materials: Properties and Applications, John Wiley & Sons, 2013. (e) M. A. Halcrow, *Chem. Soc. Rev.*, 2011, **40**, 4119-4142. (f) J. Olguin and S. Brooker, *Coord. Chem. Rev.*, 2011, **255**, 203-240. (g) A. B. Gaspar, M. Seredyuka, *Coord. Chem. Rev.*, 2014, **268**, 41-58. (h) P. Gütlich, A. B. Gaspar and Y. Garcia, *Beilstein J. Org. Chem.*, 2013, **9**, 342-391. (i) S. Brookera, *Chem. Soc. Rev.*, 2015, **44**, 2880-2892.

3 see for some examples: (a) J. A. Kitchen and S. Brooker, *Coord. Chem. Rev.*, 2008, **252**, 2072-2092. (b) B. Weber, *Coord. Chem. Rev.*, 2009, **253**, 2432-2449. (c) M. C. Muñoz and J. A. Real, *Coord. Chem. Rev.*, 2011, **255**, 2068-2093. (d) M. A. Halcrow, *New J. Chem.*, 2014, **38**, 1868-1882. (e) R. W. Hogue, R. G. Miller, N. G. White, H. L. C. Feltham, G. N. L. Jameson and S. Brooker, *Chem. Commun.*, 2014, **50**, 1435-1437. (f) G. A. Craiga, O. Roubeaub and G. Aromí, *Coord. Chem. Rev.*, 2014, **269**, 13-31.

4 (a) Y. Hasegawa, K. Takahashi, S. Kume and H. Nishihara, *Chem. Commun.*, 2011, **47**, 6846-6848. (c) K. Takahashi, Y. Hasegawa, R. Sakamoto, M. Nishikawa, S. Kume, E. Nishibori and H. Nishihara, *Inorg. Chem.*, 2012, **51**, 5188-5198.

5 (a) K. Sénéchal-David, N. Zaman, M. Walko, E. Halza, E. Rivière, R. Guillot, B. L. Feringa and M.-L. Boillot, *Dalton Trans.*, 2008, 1932-1936. (b) M. Nihei, Y. Suzuki, N. Kimura, Y. Kera and H. Oshio, *Chem. Eur. J.*, 2013, **19**, 6946-6949. (c) M. Milek, F. W. Heinemann and M. M. Khusniyarov, *Inorg. Chem.*, 2013, **52**, 11585-11592. (c) S. Venkataramani, U. Jana, M. Dommaschk, F. D. Sönnichsen, F. Tuczek, R. Herges, *Science*, 2011, **331**, 445-448.

6 (a) G. J. Halder, C. J. Kepert, B. Moubaraki, K. S. Murray and J. D. Cashion, *Science*, 2002, **298**, 1762-1765. (b) M. Ohba, K. Yoneda, G. Agustí, M. C. Muñoz, A. B. Gaspar, J. A. Real, M. Yamasaki, H. Ando, Y. Nakao, S. Sakaki and S. Kitagawa, *Angew. Chem. Int. Ed.*, 2009, **48**, 4767-4771. (c) P. D. Southon, L. Liu, E. A. Fellows, D. J. Price, G. J. Halder, K.W. Chapman, B. Moubaraki, K. S. Murray, J.-F. Létard and C. J. Kepert, *J. Am. Chem. Soc.*, 2009, **131**, 10998-11009. (d) R. Ohtani, K. Yoneda, S. Furukawa, N. Horike, S. Kitagawa, A. B. Gaspar, M. C. Muñoz, J. A. Real and M. Ohba, *J. Am. Chem. Soc.*, 2011, **133**, 8600-8605; (e) F. J. Muñoz-Lara, A. B. Gaspar, D. Aravena, E. Ruiz, M. C. Muñoz, M. Ohba, R. Ohtani, S. Kitagawa and J. A. Real, *Chem. Commun.*, 2012, **48**, 4686-4688. (f) X. Bao, H. J. Shepherd, L. Salmon, G. Molnár,

M.-L. Tong, A. Bousseksou, *Angew. Chem. Int. Ed.*, 2013, **52**, 1198-1202. (g) X.-Y. Chen, R.-B. Huang, L.-S. Zheng and J. Tao, *Inorg. Chem.*, 2014, **53**, 5246-5252. (h) M. Yamada, H. Hagiwara, H. Torigoe, N. Matsumoto, M. Kojima, F. Dahan, J.-P. Tuchagues, N. Re and S. Iijima, *Chem. Eur. J.* 2006, **12**, 4536-4549. (i) Z. Ni, M. P. Shores, *Inorg. Chem.* 2010, **49**, 10727-10735. (j) C. Lochenie, W. Bauer, A. P. Railliet, S. Schlamp, Y. Garcia and B. Weber, *Inorg. Chem.,* 2014, **53**, 11563-11572. (k) R. Kulmaczewski, J. Olguín, J. A. Kitchen, H. L. C. Feltham, G. N. L. Jameson, J. L. Tallon and S. Brooker, J. Am. Chem. Soc., 2014, 136, 878-881.

7 (a) A. Royant, K. Edman, T. Ursby, E. Pebay-Peyroula, E. M. Landau and R. Neutze, *Nature*, 2000, **406**, 645-648. (b) K.-D. Kreuer, S. J. Paddison, E. Spohr and M. Schuster, *Chem. Rev.*, 2004, **104**, 4637-4678. (c) G. A. Voth, *Acc. Chem. Res.*, 2006, **39**, 143-150.

8 (a) S.-L. Li and Q. Xu, *Energy Environ. Sci.*, 2013, **6**, 1656-1683. (b) T. Yamada, K. Otsubo, R. Makiura and H. Kitagawa, *Chem. Soc. Rev.*, 2013, **42**, 6655-6669. (c) M. Yoon, K. Suh, S. Natarajan and K. Kim, *Angew. Chem. Int. Ed.*, 2013, **52**, 2688-2700. (d) P. Ramaswamy, N. E. Wong and G. K. H. Shimizu, *Chem. Soc. Rev.*, 2014, **43**, 5913-5932.

9 (a) T. Yamada, M. Sadakiyo and H. Kitagawa, *J. Am. Chem. Soc.*, 2009, **131**, 3144-3145. (b) M. Sadakiyo, T. Yamada and H. Kitagawa, *J. Am. Chem. Soc.*, 2009, **131**, 9906-9907. (c) H. Okawa, A. Shigematsu, M. Sadakiyo, T. Miyagawa, K. Yoneda, M. Ohba, H. Kitagawa, *J. Am. Chem. Soc.*, 2009, **131**, 13516-13522. (d) M. Sadakiyo, T. Yamada and H. Kitagawa, *J. Am. Chem. Soc.*, 2014, **136**, 13166-13169.

10 (a) S. C. Sahoo, T. Kundu and R. Banerjee, *J. Am. Chem. Soc.*, 2011, **133**, 17950-17958. (b) T. Kundu, S. C. Sahoo and R. Banerjee, *Chem. Commun.*, 2012, **48**, 4998-5000. (c) T. Panda, T. Kundu and R. Banerjee, *Chem. Commun.*, 2013, **49**, 6197-6199.

11 (a) J. M. Taylor, R. K. Mah, I. L. Moudrakovski, C. I. Ratcliffe, R. Vaidhyanathan and G. K. H. Shimizu, *J. Am. Chem. Soc.*, 2010, **132**, 14055-14057. (b) S. Kim, K. W. Dawson, B. S. Gelfand, J. M. Taylor and G. K. H. Shimizu, *J. Am. Chem. Soc.*, 2013, **135**, 963-966. (c) J. M. Taylor, K. W. Dawson and G. K. H. Shimizu, *J. Am. Chem. Soc.*, 2013, **135**, 1193-1196. (d) S.-S. Bao, K. Otsubo, J. M. Taylor, Z. Jiang, L.-M. Zheng and H. Kitagawa, *J. Am. Chem. Soc.*, 2014, **136**, 9292-9295.

12 E. Pardo, C. Train, G. Gontard, K. Boubekeur, O. Fabelo, H. Liu, B. Dkhil, F. Lloret, K. Nakagawa, H. Tokoro, S. Ohkoshi and M. Verdaguer, *J. Am. Chem. Soc.*, 2011, **133**, 15328-15331.

13 (a) T. Panda, T. Kundu and R. Banerjee, *Chem. Commun.*, 2012, **48**, 5464-5466. (b) S. S. Nagarkar, S.M. Unni, A. Sharma, S. Kurungot and S. K. Ghosh, *Angew. Chem. Int. Ed.*, 2013, **53**, 2638-2642.

14 (a) S. Bureekaew, S. Horike, M. Higuchi, M. Mizuno, T. Kawamura, D. Tanaka, N. Yanai and S. Kitagawa, *Nat. Mater.*, 2009, **8**, 831-836. (b) S. Horike, D. Umeyama, M. Inukai, T. Itakura and S. Kitagawa, *J. Am. Chem. Soc.*, 2012, **134**, 7612-7615.

15 J. A. Hurd, R. Vaidhyanathan, V. Thangadurai, C. I. Ratcliffe, I. L. Moudrakovski and G. K. H. Shimizu, *Nat. Chem.*, 2009, **1**, 705-710.

16 (a) D. Samanta and P. S. Mukherjee, *Chem. Eur. J.*, 2014, **20**, 12483-12492. (b) D. Samanta and P. S. Mukherjee, *Chem. Commun.*, 2014, **50**, 1595-1598.

17 J. Luan, J. Zhou, Z. Liu, B. Zhu, H. Wang, X. Bao, W. Liu, M. L. Tong, G. Peng, H. Peng, L. Salmon and A. Bousseksou, *Inorg. Chem.*, 2015, **54**, 5145-5147.

18 (a) H. Toftlund, E. Pedersen and S. Yde-Andersen, *Acta Chem. Scand.*, 1984, **A38**, 693-697. (b) J.-F. Létard, S. Asthana, H. J. Shepherd, P. Guionneau, A. E. Goeta, N. Suemura, R. Ishikawa and S. Kaizaki, *Chem. Eur. J.*, 2012, **18**, 5924-5934.

19 T. Buchen, H. Toftlund and P. Gütlich, *Chem. Eur. J.*, 1996, **2**, 1129-1133.

20 (a) C. P. Berlinguette, A. Dragulescu-Andrasi, A. Sieber, H.-U. Güdel, C. Achim and K. R. Dunbar, *J. Am. Chem. Soc.*, 2005, **127**, 6766-6779. (b) M. Nihei, Y. Sekine, N. Suganami, K. Nakazawa, A. Nakao, H. Nakao, Y. Murakami and H. Oshio, *J. Am. Chem. Soc.*, 2011, **133**, 3592-3600.

21 (a) G. S. Matouzenko, A. Bousseksou, S. Lecocq, P. J. Van Koningsbruggen, M. Perrin, O. Kahn and A. Collet, *Inorg. Chem.*, 1997, **36**, 2975-2981. (b) G. S. Matouzenko, A. Bousseksou, S. Lecocq, P. J. Van Koningsbruggen, M. Perrin, O. Kahn and A. Collet, *Inorg. Chem.*, 1997, **36**, 5869-5879.

22 (a) P. Guionneau, M. Marchivie, G. Bravic, J.-F. Létard and D. Chasseau, *J. Mater. Chem.*, 2002, **12**, 2546-2551. (b) P. Guionneau, M. Marchivie, G. Bravic, J. F. Léetard and D. Chasseau, *Top. Curr. Chem.*, 2004, **234**, 97-128.

23 L. Infantes and S. Motherwell, *CrystEngComm*, 2002, **4**, 454-461.

24 R. G. Miller, S. Narayanaswamy, J. L. Tallon and S. Brooker, *New J. Chem.*, 2014, **38**, 1932-1941.

25 I. Šalitroš, N. T. Madhu, R. Boča, P. Pavlik and M. Ruben, *Monatsh. Chem.*, 2009, **140**, 695-733 and references therein.

26 (a) K. D. Kreuer, A. Rabenau and W. Weppner, *Angew. Chem. Int. Ed.*, 1982, **21**, 208-209. (b) T. Kundu, S. C. Sahoo and R. Banerjee, *Chem. Commun.*, 2012, **48**, 4998-5000.

27 (a) A. Böttcher, H. Elias, L. Müller and H. Paulus, *Angew. Chem. Int. Ed. Engl.*, 1992, **31**, 623-625. (b) I. Morgenstern-Badarau, F. Lambert, J. P. Renault, M. Cesario, J.-D. Maréchal and F. Maseras, *Inorg. Chim. Acta* 2000, 338-350 (c) J. Gómez, G. García-Herbosa, J. V. Cuevas, A. Arnáiz, A. Carbayo, A. Muñoz, L. Falvello and P. E. Fanwick, *Inorg. Chem.*, 2006, **45**, 2483-2493. (d) V. M. Ugalde-Saldívar, M. E. Sosa-Torres, L. Ortiz-Frade, S. Bernès and H. Höpfl, *J. Chem. Soc. Dalton Trans.*, 2001, 3099-3107. (e) J. P. Saucedo-Vázquez, V.M. Ugalde-Saldívar, A. R. Toscano, P. M. H. Kroneck and M. E. Sosa-Torres, *Inorg. Chem.*, 2009, **48**, 1214-1222. (f) C. J. Christian, A. Arbuse, X. Fontrodona, M. A. Martinez, A. Llobet and F. Maseras, *Dalton Trans.*, 2009, 6013-6020. (g) R. K. Wilson and S. Brooker, *Dalton Trans.*, 2013, **42**, 12075-12078.

28 (a) S. Bonnet, M. A. Siegler, J. S. Costa, G. Molnár, A. Bousseksou, A. L. Spek, P. Gamez and J. Reedijk, *Chem. Commun.*, 2008, **43**, 5619-5621. (b) Z. Arcis-Castíllo, S. Zheng, M. A. Siegler, O. Roubeau, S. Bedoui and S. Bonnet, *Chem. Eur. J.*, 2011, **17**, 14826-14836. (c) S. Zheng, M. A. Siegler, O. Roubeau, S. Bonnet, *Inorg. Chem.*, 2014, **53**, 13162-13173.

29 K. Michelsen, *Acta Chem. Scand.* 1977, **A31**, 429-436.

In air a spin crossover active iron(II) complex of amine/NCBH3− ligands is converted to a low spin complex of imine/CN− ligands

ABSTRACT

Two new mononuclear Fe^{II} complexes, $[FeL_1(NCBH_3)_2]$ (**1**) and $[FeL_2(CN)_2]\cdot 3H_2O$ (**2**) (L_1 = N,N'-bis(2-pyridylmethyl)-1,2-ethanediamine, L_2 = N-(2-pyridylmethyl)-N'-(2-pyridylmethylene)-1,2-ethanediamine) were synthesized from the same starting solution under different atmospheric conditions. Complex **1** was isolated in N_2 atmosphere with an expected molecular structure, namely a tetradentate L_1 ligand and two $NCBH_3^-$ co-ligands wrapping an iron(II) ion. It exhibits gradual spin crossover centered around 355 K, as confirmed by X-ray crystallography, magnetic, DSC and Mössbauer studies. Complex **2** was isolated in the presence of air. One of the secondary amine groups in L_1 undergoes an in-situ oxidative dehydrogenation, forming a new monoimine asymmetric ligand L_2. Besides, CN^- co-ligand is also in-situ generated from $NCBH_3^-$ during the reaction. The strong ligand field strength imposed by CN^- and L_2 stabilizes **2** in LS state. Solvent water molecules in complex **2** are hydrogen bonded into a well-defined 1D water chain. **2** shows a proton conductivity of 8.9×10^{-5} S cm^{-1} at 55 °C and 95 % relative humidity.